Journal of Energy Storage 73 (2023) 108804

Contents lists available at ScienceDirect

Journal of Energy Storage

journal homepage: www.elsevier.com/locate/est

Research Papers

Investigations on substituted Si-doped Mn_2O_3/Mn_3O_4 redox pair for thermochemical energy storage

Yan Huang [a], Peiwang Zhu [a], Changdong Gu [b], Haoran Xu [a], Jinsong Zhou [a], Gang Xiao [a,*]

[a] State Key Laboratory of Clean Energy Utilization, College of Energy Engineering, Zhejiang University, Hangzhou, Zhejiang 310027, China
[b] State Key Laboratory of Silicon Materials, College of Materials Science and Engineering, Zhejiang University, Hangzhou, Zhejiang 310027, China

ARTICLE INFO

Keywords:
Thermochemical energy storage
Manganese oxide
Doped mental oxides
Redox reaction
Density functional theory

ABSTRACT

Next-generation concentrated solar power plants with thermochemical energy storage can meet the demand for peak regulation and power supply, which stimulates the development and application of low-priced metal oxide thermochemical thermal storage materials. Mn-based composite metal oxide is a competitive candidate for large-scale applications given its character of being non-toxic, cheap, and highly efficient. However, the utilization of pure Mn_2O_3 suffers from sintering, which limits its re-oxidation and hence affects the applicability. In this study, Si is introduced to solve the above problems and improve the reaction characteristics of pure Mn_2O_3. $(Mn_{1-x}Si_x)_2O_3$ is synthesized by substituent doping, with the best performance at x = 3 % and 5 %, reaching 96.18 % and 94.71 % of reduction conversion rate, respectively. The performance decay of the $(Mn_{0.95}Si_{0.05})_2O_3$ sample was tested and evaluated, with reduction conversions of 90.92 % and 63.64 % after 50 and 300 cycles, respectively. A series of characterization results confirm that Si^{4+} is successfully doped into the Mn_2O_3 lattice, introducing defects into the crystal structure, which is favorable for the oxidation reaction. Density functional theory calculations of oxygen adsorption/dissociation and oxygen diffusion indicate that the doped Mn-Si oxides have lower reaction potentials and energies, which explains the promotion of the re-oxidation reaction by Si. By investigating the thermochemical energy storage properties and mechanism of Mn-Si composite metal oxides, we provide guidance for large-scale, cheap, and eco-friendly energy storage applications.

1. Introduction

Thermochemical energy storage (TCES) is of enormous potential in supporting next-generation concentrated solar power (CSP) plants to meet the requirement of peak load regulation and provide electricity on demand [1]. Compared to sensible heat storage materials commonly implemented in commercial CSP plants, TCES materials are competitive in terms of storage density and operation temperature (700–1500 °C), enabling higher power generation efficiency and lower operating costs for CSP plants [2]. In addition, metal oxide systems based on reversible endothermic-exothermic redox reactions possess a wide variety of advantages, including abundant raw materials, high reaction enthalpy, fast reaction kinetics [3], and no need for gas storage [4].

Among numerous metal oxide redox pairs, Co_3O_4/CoO [5–7], CuO/Cu_2O [8–10], Mn_2O_3/Mn_3O_4 [11], have received the most attention in TCES field. Co_3O_4/CoO pair was intensively investigated in early studies because of its high energy storage density and completely reversible reaction. Nevertheless, high material costs and toxicity impede its practical application [5,6,12]. The operation temperature of CuO/Cu_2O pair is close to the melting points of Cu_2O (1235 °C) [1], leading to severe sintering and poor kinetics [13]. Mn_2O_3/Mn_3O_4 pair is inexpensive and environmentally friendly but the re-oxidation is difficult to occurs [14,15], which is because sintering inhibits oxygen diffusion [16]. Previous studies have found that re-oxidation properties of Mn_2O_3/Mn_3O_4 pair can be improved to varying degrees by doping a range of cations, including Fe^{3+} [17], Mg^{2+} [18], and Cu^{2+} [19].

The initial trial on doping modification of Mn_2O_3/Mn_3O_4 is to add iron [15], which allows the formation of stable solid solutions due to the similar ionic radius of Mn^{3+} and Fe^{3+}, and effectively avoids the particle sintering of pure Mn_2O_3 during the reaction. Carrillo et al. and Xiang et al. obtained commendable thermal performances by doping 20 mol% Fe, which forms a uniform solid solution $(Mn_{0.8}Fe_{0.2})_2O_3$ [11,20]. Due to the formation of the core-shell structure $MnFe_2O_4@Mn_{2.7}Fe_{0.3}O_4$ at reduced state, the oxidation energy barrier of the core $MnFe_2O_4$ is

* Corresponding author.
E-mail addresses: yanhuang@zju.edu.cn (Y. Huang), zhupw@zju.edu.cn (P. Zhu), cdgu@zju.edu.cn (C. Gu), haoranxu@zju.edu.cn (H. Xu), zhoujs@zju.edu.cn (J. Zhou), xiaogangtianmen@zju.edu.cn (G. Xiao).

https://doi.org/10.1016/j.est.2023.108804
Received 5 February 2023; Received in revised form 16 August 2023; Accepted 21 August 2023
Available online 7 September 2023

drastically reduced, enabling re-oxidation reaction to complete in a few minutes [20]. Randhir et al. investigated the performance of Mn-Mg composite oxide thermochemical materials with Mn/Mg molar ratios of 2/3, 1/1, and 2/1 and tested the cycling stability for 10 redox cycles between 1200 °C and 1500 °C [18,21,22]. Solid-state thermochemical fuels based on magnesium manganese oxides can provide high-temperature (>1000 °C) energy storage/releasing capabilities across seasons and are also cost-effective [23]. Hlongwa et al. proposed Cu-Mn composite spinel type oxide $CuMn_2O_4$, and verified the stable cycling performance between 900 and 1000 °C through 5 cycles [24]. The reaction enthalpy of $CuMn_2O_4$ under air and argon atmosphere is 14 kJ/kg and 144 kJ/kg [24], respectively. Generally speaking, the heteroatom doping ratios in existing studies are usually not <20 %, so new substances are formed during the reaction to alleviate the sintering problem.

In this work, we modified Mn_2O_3/Mn_3O_4 pair by doping with a low percentage of Si elements to investigate the inhibition of sintering by cationic substitution doping as well as its modification mechanism. Compared to the above-mentioned elements, Si is second only to oxygen on the Earth's surface, occupying nearly 28 %, which is cheap and non-toxic [25]. Shulman et al. developed Mn-Si composite metal oxides based on chemical looping and CO_2 capture with SiO_2 doping ratio of 20 wt%, which performed unsatisfactory reversibility under 10 % O_2 in N_2 [26]. Bielsa et al. [25] and D. Yilmaz et al. [27] firstly applied Mn-Si oxides to the TCES field, and investigated the reversibility of redox reactions at lower Si doping ratios. Bielsa et al. demonstrated the effect of Si doping at 1 mol% and 5 mol% by dry method and sol-gel method, respectively, and verified the improvement of Si^{4+} on the cyclic behavior of material re-oxidation rate by 40 redox cycles [25]. It was found that the sintering rate in Mn_2O_3 is governed by the ionic grain boundary diffusion rate, and the segregation of Si^{4+} dopant at the grain boundary would hinder the ionic grain boundary diffusion rate [25]. In subsequent work, $(Mn_{0.99}Si_{0.01})_2O_3$ was preferentially selected for the reaction kinetics study, and kinetic parameter models for the reduction and oxidation reactions were obtained, both of that were determined to be controlled by nucleation and growth mechanisms [28]. The work of Yilmaz elaborated that at from 2 to 30 wt% Si content, Mn_2O_3 could react continuously with SiO_2, with an optimal reactivity material doping of 6 wt%. When composed of 30 wt% SiO_2, side reactions occurred to generate $MnSiO_3$ that is stable at high temperatures unfavorable to the oxygen coupling-uncoupling ability [27].

Existing research has applied Mn-Si composition metal oxides in chemical-looping combustion with oxygen uncoupling. Still, there are much fewer studies in the field of TCES, which remain mainly in the reactive characters, with less exploration of the microscopic level and a need of long-cycle tests for heat storage and discharge. This study investigated Si^{4+} substitutional doped in Mn_2O_3/Mn_3O_4 pair with no >10 mol% and verified the successful incorporation of Si into the lattice by a series of characterization means. In terms of storage and exothermic performance, redox properties were studied by STA (simultaneous thermal analyzers). Over 300 cycles in the reaction temperature region and corresponding microscopic morphological evolution were also studied. In addition, the bonding of Mn-Si-O as well as its microscopic mechanism were also explored, and the reaction and diffusion energy barriers of $(Mn_{1-x}Si_x)_2O_3$ during the redox were computed based on density functional theory (DFT). Through this study, we seek to investigate a cheaper and more environmentally friendly TCES material, and provide a guideline for future large-scale applications of thermochemical energy storage in CSP.

2. Experimental section

2.1. Material preparation

The Mn-Si composite metal oxide with the molecular formula $(Mn_{1-x}Si_x)_2O_3$ ($0 \leq x \leq 0.15$) was synthesized using the sol-gel method. $Mn(NO_3)_2$ (50 %, Sinopharm) and $Si(C_8H_{20}O_4)$ (Silicon acetate, 98 %, Sigma Aldrich) were dissolved in 200 mL of deionized (DI) water under magnetic stirring to afford a homogeneous solution, and citric acid (AR, Sinopharm) at a molar proportion of 1:5 was added into the mixture. After stirring for 2 h, the ethylene glycol (AR, Sinopharm) with 2/3 mole ratio to citric acid was added. The solution was kept under stirring for another 3 h. When the gel was formed, the gelatinous mixture was dried at 200 °C for 3 h, and then calcined at 450 °C and 800 °C for 2 h and 4 h, respectively.

2.2. Characterization techniques

Structural analysis of the material was carried out by X-ray powder diffraction (XRD) using a PANalytical B.V. (Netherland) X-pert Powder diffractometer (Cu Kα radiation). The data were collected at room temperature between 10° and 80° in 2θ with a step size of 0.02° and a counting time of 30s per angel. The MDI Jade 9.0 software was used to determine the phase composition of the material. The crystal phases were identified by using the ICDD PDF-4 database. The Fourier transform infrared spectra (FTIR) of the as-synthetic samples were recorded in the mid-IR frequency region at 4000–400 cm^{-1} using Nicolet iS20 infrared spectrometer from Thermo Scientific at 4 cm^{-1} resolution. Thermogravimetric analysis (TGA) and differential scanning calorimetry (DSC) measurements were performed with TGA/DSC3+ simultaneous thermal analyzer (METTLER TOLED) at air atmosphere. In redox property and cyclability studies, 10 mg of sample were placed into alumina crucibles and subjected to charging and discharging cycles between 650 °C and 1000 °C under air atmosphere. The prepared samples were imaged by means of a SU-8010 field-emission scanning electron microscope (SEM) to investigate the particle morphologies and energy-dispersive X-ray spectroscopy (EDS) analysis was carried out to obtain chemical composition maps of the different observed sample zones. The X-ray photoelectron spectroscopy (XPS) measurements were carried out using a Thermo Scientific K-Alpha spectrometer by using Al Ka (1486.6 eV) radiation as the excitation source. Samples were corrected by setting the binding energy (BE) maximum of the adventitious carbon (C 1s) at 284.6 eV. The XPS analysis was performed at room temperature with pressures $<10^{-8}$ Pa. The samples were outgassed in a vacuum oven overnight before XPS measurements. Scanning transmission electron microscopy (STEM) equipped with selected area electron diffraction (SAED) analysis was employed to visualize the crystallinity, microstructure, and distribution of different elements at different stages, which were carried out on a Hitachi HT-7700 transmission electron microscopy system operated at 100 kV.

2.3. Calculation methods

Vienna Ab-initio Simulation Package (VASP) was adopted to perform density functional theory calculations [29,30]. The core electrons were represented by the projector augmented wave (PAW)method [31], and the Kohn-Sham equations were solved by the generalized gradient approximation (GGA), and the Perdew-Burke-Ernzerhof (PBE) exchange-correlation functional [32]. The plane-wave basis set was obtained for valence electrons with a kinetic energy cutoff of 450 eV. The low-index surfaces Mn_3O_4 (100) and $(Mn_{0.95}Si_{0.05})_3O_4$ (100) are selected to investigate the O_2 adsorption, dissociation as well as O anion migrations [20], and detailed test data is presented in Table S1. The vacuum layer is set to build the slab model, and we choose a vacuum layer with a thickness of 12 Å in the z-direction to avoid spurious interactions between adjacent slabs. Concerning the Mn_3O_4 (100) and $(Mn_{0.95}Si_{0.05})_3O_4$ (100) slabs, the sampling of the Brillouin zone by $4 \times 3 \times 1$ and $5 \times 4 \times 1$ k-point grids were tested under the Monkhorst-Pack scheme [33], respectively, and it was found that the use of $4 \times 3 \times 1$ k points could reduce the number of operations while satisfying the computational accuracy. The structural relaxation was performed in accordance with the Hellmann-Feynman approximation, whereas the

atomic positions were relaxed to the extent that the force acting on each atom was <0.02 eV/Å. To describe the strongly correlated electrons in manganese, the DFT + U method was employed, where the introduced Hubbard parameter "U" altered the self-interaction error of the electrons and enhanced the description of the correlation effect [34,35]. Accordingly, U = 2.0 eV was used for the Mn(3d) orbitals in metal oxides [20]. The energy barriers for V_O diffusion and oxygen adsorption/dissociation were computed using the climbing-image nudged elastic band (CI-NEB) method implemented in VASP. CI-NEB includes the simultaneous calculation of several coupled structural optimizations (images) along the diffusion paths linking the initial and final states [36].

3. Results and discussion

3.1. Structure and composition of substitution doping of Si

The composition and crystalline properties of the samples are summarized in Table 1. The composition of samples with different Si doping ratios is obtained from the X-Ray powder diffraction (XRD) patterns (Fig. 1), which is well fitted with the Mn-Si-O phase diagram (Fig. S1) under respective proportions and synthetized temperature. The XRD patterns of 1 %–7 % Si-doped samples exhibited only the reflections typical of (211), (222), (400), (332), (431), (440), and (622) planes corresponding to the characteristic defective structure of the cubic Mn_2O_3 (ICCD#00-031-0825 bixbyite). Further, by enlarging the 32°–34° region of the XRD pattern, it can be found that the diffraction peaks of samples with different doping ratios are slightly shifted to the right compared with the standard values, stating that the lattice parameters of the synthesized samples are smaller than the un-doped sample. Since the doped ionic radius of Si^{4+} (0.4 Å) in six-fold coordination is smaller than that of Mn^{3+} (0.645 Å), that is, Si^{4+} is incorporated into the lattice of Mn_2O_3 by sol-gel method, thereby forming stable solid solutions $(Mn_{1-x}Si_x)_2O_3$. As shown in Table 1, a slight decrease in the lattice parameter can be observed with the increase in the doping ratio. This observation is coherent with Vegard's law, which states a linear relationship between the lattice parameters and the concentration of its constituent elements at a constant temperature [37]. The grain size of different samples can be calculated using jade 9.0, whose values are very close to the literature, and the results are shown in Table 1. The half-height widths of multiple characteristic diffraction peaks were measured, then the data points were linearly fitted by least squares, and their particle sizes were calculated by Hall's method. In this way, we can obtain that the average particle size of different samples ranges from 103 nm to 127 nm. In particular, when the doping ratio of Si exceeds 10 mol%, Si will not be completely incorporated into the lattice, and a new complex Mn_7SiO_{12} will be generated. Mn_7SiO_{12} does exist though its characteristic peak in XRD patterns is not obvious since its characteristic peak coincides with that of Mn_2O_3. By using Jade 9.0, Mn_7SiO_{12} content could be analyzed at about 1.5 wt%. Studies related to phases such as $MnSiO_3$ and Mn_7SiO_{12} have shown that the presence of these phases is undesirable since they present different reaction parameters [25,27]. Thus, the samples whose doping ratio beneath 10 mol% were chosen for further study.

Table 1
Material identification, doping composition, composition of the synthesized samples, and lattice parameter.

Sample	Si (mol %)[a]	Composition	Lattice parameter a (Å)	Average crystallite size (nm)
Mn_2O_3	0	Mn_2O_3	9.430	128
$(Mn_{0.99}Si_{0.01})_2O_3$	1	Mn_2O_3	9.415	127
$(Mn_{0.97}Si_{0.03})_2O_3$	3	Mn_2O_3	9.412	106
$(Mn_{0.95}Si_{0.05})_2O_3$	5	Mn_2O_3	9.410	114
$(Mn_{0.93}Si_{0.07})_2O_3$	7	Mn_2O_3	9.404	103
$(Mn_{0.9}Si_{0.1})_2O_3$	10	Mn_2O_3/ Mn_7SiO_{12}	9.415	185

[a] Si (mol%) = 100 * n(Si) / {n(Si) + n(Mn)}.

Fig. 1c displays the reduced XRD patterns of 1–5 mol% Si-doped samples, which exhibits characteristic peaks consistent with Mn_3O_4 (ICCD #01-089-4837 hausmannite). Similarly, in the low-ratio doping scenario, the reduction product of $(Mn_{1-x}Si_x)_2O_3$ is only a single phase of Mn_3O_4 with a slight shift compared to the standard card peak line, indicating that the Si element remains in the lattice during the transition of the composite metal oxide from the bixbyite to the hausmannite. After one redox cycle, the sample maintains the same crystalline phase as before the reaction (Fig. S2), thus confirming the reversibility of the redox reaction. From this we verified its reaction equation of low-doped Mn-Si composite metal oxide [25]:

$$6(Mn_{1-x}Si_x)_2O_3 \leftrightarrow 4(Mn_{1-x}Si_x)_3O_4 + O_2 \quad (1)$$

The FT-IR spectrum can provide additional evidence for the structure of $(Mn_{1-x}Si_x)_2O_3$. In order to avoid low Si content conditions where the test signal is noisy, and the peak is not obvious, pure Mn_2O_3 and $(Mn_{0.95}Si_{0.05})_2O_3$ samples were chosen for FT-IR, as shown in Fig. 2. The detailed FTIR spectra at 400–1200 cm^{-1} are presented in Fig. S2. For fresh samples of pure Mn_2O_3 (Fig. 2a) and $(Mn_{0.95}Si_{0.05})_2O_3$ (Fig. 2b), the vibrational bands located at 521, 572, and 665 cm^{-1} are referred to as the stretching vibrations of Mn-O [38,39]. And the peaks at 1045 cm^{-1} and 961 cm^{-1} shown in Fig. 2b could be attributed to the anti-symmetric stretching vibration of O-Si-O and the vibration of Si-O-Mn, respectively. The vibrational frequencies of Si-O-M (M = Ti, Fe) have been discussed in some literature [40–43], and it is generally agreed that doping of metal cations in Si-O-Si causes a vibrational band to appear at 950–970 cm^{-1} and intensity grows with increasing doping ratio. Wang [44] et al. attributed the peak appearing at 960 cm^{-1} to the vibration of the Si-O-Mn bond. Consequently, it is believed that Si ions would have been incorporated into the framework of Mn band, leading to the evident vibration of Si-O-Mn bond near 960 cm^{-1}. As for the reduction state (Fig. 2e), two obvious absorption peaks at 499 and 613 cm^{-1} were observed, which may be related to the coupling of the Mn—O stretching modes in the tetrahedral and octahedral sites. The absorption peak at 415 cm^{-1} in the 500 to 400 cm^{-1} region was a band stretching mode at the octahedral site [45], and the above three peaks are consistent with the peaks of Mn_3O_4 in the literature [46]. Furthermore, $(Mn_{0.95}Si_{0.05})_2O_3$ after 1st cycle (as is conveyed by Fig. 2c) shows corresponding peaks at around 517, 570, 666, 955, and 1041 cm^{-1}, which indicates that after redox, the sample structure is restored to the initial state and the reaction is completely reversible. Nevertheless, after the 100th redox cycle, the Si-O-Mn peak at 954 cm^{-1} is much stronger and the vibrational peak of O-Si-O is blue-shifted from 1045 cm^{-1} to 1108 cm^{-1} along with broadening in Fig. 2d, due to the silica tetrahedron formation. The stronger the chemical bonding, the higher the frequency of the peak position. The repeated heat absorption and exothermic processes lead to the formation of amorphous SiO_2 by combining part of the silicon with oxygen, which is in accordance with the shoulder peak presented at 800 cm^{-1}. Naturally, the presence of different phase will deteriorate thermal performance, which is undesirable.

Note worthily, O atoms in crystalline water are apt to coordinate with metal cations. The stronger the coordination ability of metal ions on the O—H bond, the stronger the induction of electron clouds and the stretching vibration of water molecules squint to move to the lower frequency. Usually, the wave number at 3424 cm^{-1} is the water of crystal between the compounds, and its absorption peak of bending vibration at about 1640 cm^{-1} shows 1/3 as strong as stretching vibration. So, the broad band centered at 3427 cm^{-1} as well as the peak at about 1627 cm^{-1} correspond to stretching and bending vibration of hydroxyl groups of H_2O absorbed by the samples or KBr [47], respectively.

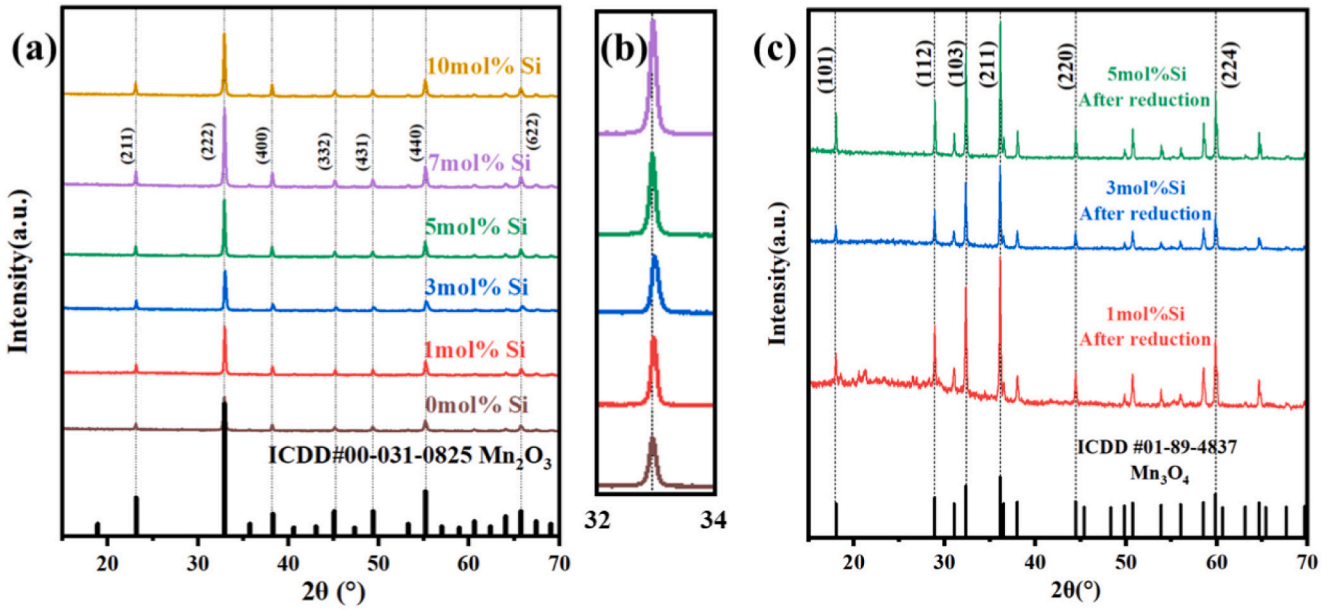

Fig. 1. XRD patterns of samples with different doping ratios: (a) in the oxidized state; (b) detail graph of the peak in 32– 34° region; (c) in the reduced state.

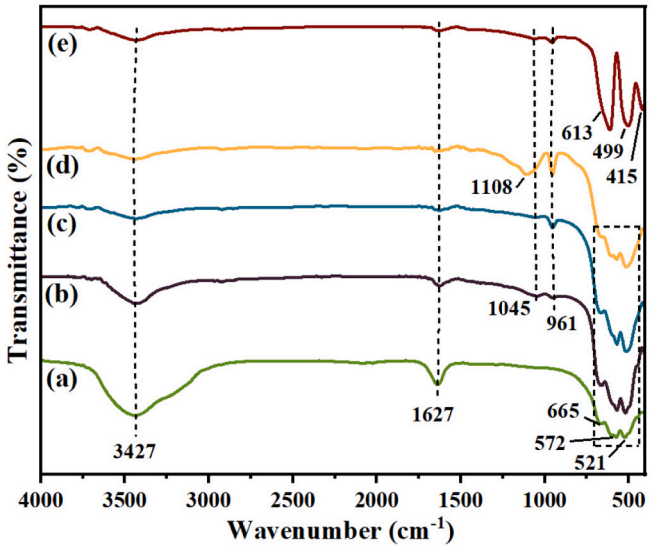

Fig. 2. FT-IR transmittance spectrum: (a) pure Mn_2O_3; (b) fresh sample of $(Mn_{0.95}Si_{0.05})_2O_3$; (c) $(Mn_{0.95}Si_{0.05})_2O_3$ after 1st re-oxidation; (d) $(Mn_{0.95}Si_{0.05})_2O_3$ after 100th redox; (e) $(Mn_{0.95}Si_{0.05})_2O_3$ after 1st reduction.

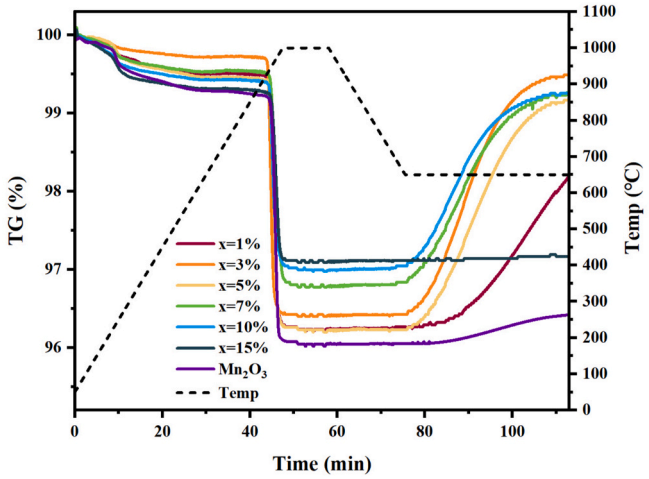

Fig. 3. TG curves of fresh samples with different doping ratios.

3.2. Thermal performance

The degree of redox reactions is a vital indicator of heat absorption and discharge for thermochemical thermal storage materials. In this study, the degree of reaction of the samples was obtained by the simultaneous thermal analyzer (STA) at 650–1000 °C (50 mL min^{-1}). The temperature was first ramped up to 1000 °C at a rate of 20 °C min^{-1}, which is a sufficient temperature for the reduction reaction. In order to ensure the entire progress of the reduction reaction and avoid unnecessary sintering caused by higher temperature [48], the temperature is maintained at 1000 °C for 10 min. The cooling down process was also carried out at a rate of 20 °C min^{-1} until 650 °C, which is the temperature at which the oxidation reaction of the Mn-Si composite oxide can occur rapidly. The isothermal condition for 40 min was maintained to ensure the completion of oxidation. As presented in Fig. 3, the oxidation rate of Mn_2O_3 is 0.24 wt% over a period of >50 min, indicating a need to improve the kinetics of the oxidation reaction. In this study, samples doped with 1 to 10 mol% Si could all improve the re-oxidation rate to varying degrees, while the reaction performance decreased with doping ratios above 10 % (Fig. 3). Notably, the reduction rate diminishes with the increment of Si percentage, while the re-oxidation rate follows the same trend as the exothermic enthalpy, increasing at first and then decreasing. That is because the low Si content of $(Mn_{0.99}Si_{0.01})_2O_3$ makes it behave similarly to pure Mn_2O_3 with a relatively slow oxidation rate [49]; nevertheless, too high content of Si leads to the formation of Braunite $3Mn_2O_3{\cdot}MnSiO_3$, which is a more stable manganese silicate in the reaction temperature region and results in a decrease in mass loss [25]. Carrillo et al. [50] demonstrated that Mn^{2+} ions on the tetrahedral sites are the main species involved in the oxidation process. Due to the incorporation of a smaller radius (0.4 Å) Si^{4+}, the Mn^{2+}-O bond length increases, and the bond strength weakens [25], making it easier for bond breaking and electron migration during the oxidation process.

From Table 2, it can be seen that $(Mn_{0.97}Si_{0.03})_2O_3$ and $(Mn_{0.95}Si_{0.05})_2O_3$ exhibit excellent redox performance with mass losses of 3.27 % and 3.22 %, whose reduction conversion rates are up to 96.18 % and 94.71 %, respectively. And their re-oxidation conversion rates are

Table 2
Thermal performance of $(Mn_{1-x}Si_x)_2O_3$ samples.

Sample	x	T_{red} (°C)	Reduction rate (%)	Δt_{red} (min)	T_{ox} (°C)	Oxidation rate (%)	Δt_{ox} (min)	Thermal storage (kJ/kg)
Mn_2O_3	0	937	3.36	3.7	678	0.24	>50	197.6
$(Mn_{0.99}Si_{0.01})_2O_3$	1 %	920	3.27	4.6	683	1.91	>30	139.5
$(Mn_{0.97}Si_{0.03})_2O_3$	3 %	916	3.27	4.2	702	3.07	21	189.8
$(Mn_{0.95}Si_{0.05})_2O_3$	5 %	924	3.22	3.5	707	2.93	20	183.9
$(Mn_{0.93}Si_{0.07})_2O_3$	7 %	931	2.82	4.6	724	2.45	22	172.9
$(Mn_{0.9}Si_{0.1})_2O_3$	10 %	932	2.44	5.1	719	2.28	19	161.5
$(Mn_{0.85}Si_{0.15})_2O_3$	15 %	940	2.21	3.8	–	–	–	154.7

90.29 % and 86.18 %, respectively, reflecting their good reversibility. The reduction time Δt_{red} of the doped samples did not change substantially compared with that of pure Mn_2O_3, with an average reduction time of 4.3 min and a slight difference in accordance with the amount of doping. For the samples with Si doping amount of 3 %–10 %, the re-oxidation time Δt_{ox} was all around 20 min. Moreover, the trend of the reaction enthalpy with the doping amount is rising, followed by descending, and reaches a maximum value at x = 3 %. Fig. S4 shows that the reduction enthalpy for $(Mn_{0.97}Si_{0.03})_2O_3$ is 189.8 kJ/kg while that of re-oxidation is 179.9 kJ/kg.

The morphological differences between Mn-Si oxides with different doping ratios and commercial Mn_2O_3 can be observed by scanning electron microscopy (SEM), as presented in Fig. 4. The corresponding particle size distribution statistics are shown in Fig. S5, and the average particle size is consistent with the calculation results of jade 9.0 (shown in Table 1). Commercial Mn_2O_3 shows a typical coral-like shape with relatively small pores, while the morphology remains basically the same as Mn_2O_3 when the Si-doped content is low (<5 %). However, when the doping rate reaches 10 %, the morphologies become flattened like lotus leaves stacked on top of each other, while at x = 15 %, the structures are denser with almost no holes. This is attributed to the formation of new products or the precipitation of SiO_2, and the small specific surface area is not conducive to gas diffusion and hinders the redox reaction, which can explain the decrease of the reaction rate shown in Fig. 3.

3.3. Thermochemical cycling behavior

The application of TCES materials needs to consider the ability to store and release heat over a long period. In the existing TCES studies, the Mn-Si oxides were tested up to 80 cycles [28], while the present research cycled for up to 300 cycles to observe the degree of decay. The TG curves and morphological changes of $(Mn_{0.95}Si_{0.05})_2O_3$ after long-term cycles are shown in Fig. 5, and the corresponding data are summarized in Table 3. Redox cyclic testing was performed in an air atmosphere (50 mL min^{-1}) between 650 °C and 1000 °C. The TG data of the first reaction showed that the reduction reaction could be completed in a few minutes under these conditions. Thus, the temperature was first raised to 1000 °C at a rate of 20 °C min^{-1}, then immediately cooled to 650 °C at the same rate and held in isothermal conditions for 30 min. As for the aging process, the sample powder is placed in a Muffle furnace for redox cycling between 650 °C and 1000 °C. In order to ensure the full reaction of the sample, stay in the reduction temperature and oxidation temperature section for 30 min each. Every completed reduction and then oxidation is regarded as a cycle. As the number of cycles increases, the reduction temperature remains almost unchanged while the onset temperature of re-oxidation increases. Owing to the sintering phenomenon after the redox cycle test, the pores become larger and the specific surface area decreases, which is not conducive to the diffusion of gas. When the gas-solid reaction enters the product layer diffusion phase, where the reaction rate is low, a higher reaction temperature is required to bring the reaction back to the fast reaction phase [51].

The performance degradation was less pronounced in the first 50 cycles, and the reduction reaction conversion remained above 90 %, with a re-oxidation conversion of 82.74 %. Compared with Fig. 5b, the microscopic morphology shown in Fig. 5c is similar, but there is some growth in the average grain size from 0.105 μm to 0.254 μm after 50 cycles. After 100 cycles, significant grain growth occurs and the average particle size is 0.621 μm. Accordingly, a more obvious decay in conversion occurs compared to the first 50 cycles. The conversion rate decreased from 90.92 % to 77.66 %, which may be ascribed to grain growth and precipitation of Si elements (consistent with the analysis results of FTIR spectra in Fig. 2). The overall morphology of the $(Mn_{0.95}Si_{0.05})_2O_3$ remained basically unchanged during 100–300 cycles, while the average grain size increased from 0.703 μm to 0.778 μm. The increase of average particle size caused by grain growth is the main reason for the deterioration of reversibility [25]. It should be noted that the weight loss of part of the samples after the initial reduction was not recovered. That could be attributed to some impurities mixed in the preparation process and Mn_2O_3 that was not successfully doped with Si, which was lost in the beginning few cycles, as observed by other authors

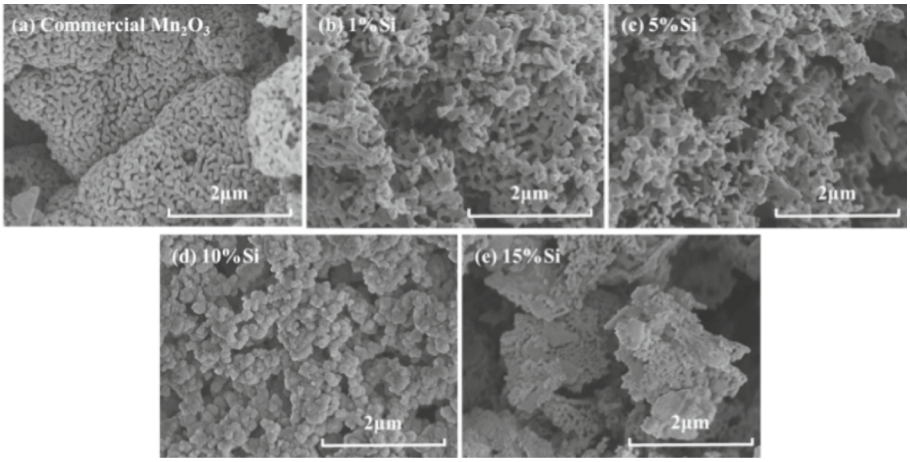

Fig. 4. SEM images of $(Mn_{1-x}Si_x)_2O_3$ samples: (a) commercial Mn_2O_3, (b) x(Si) = 1 mol%, (c) x(Si) = 5 mol%, (d) x(Si) = 10 mol%, (e) x(Si) = 15 mol%.

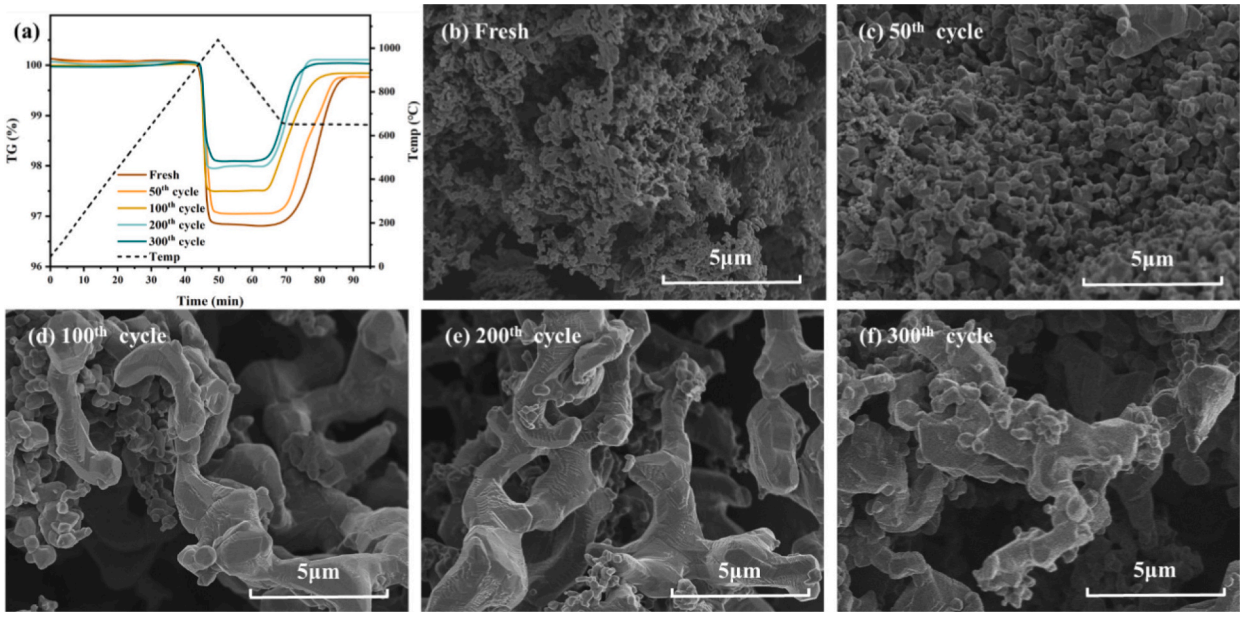

Fig. 5. Cyclicality test of $(Mn_{0.95}Si_{0.05})_2O_3$: (a) Cyclic TG curves, (b)–(f) SEM images of $(Mn_{0.95}Si_{0.05})_2O_3$ after redox cycling.

Table 3
Performance evolution of $(Mn_{0.95}Si_{0.05})_2O_3$ samples after cyclic redox reaction.

Number of cycles	Mean particle size (μm)	T_{red} (°C)	Reduction conversion (%)	T_{ox} (°C)	Re-oxidation conversion (%)
1st	0.105	924	94.71	707	86.18
50th	0.254	925	90.92	710	82.74
100th	0.621	932	77.66	741	72.22
200th	0.703	933	71.03	747	70.32
300th	0.778	935	63.46	749	62.82

[11,25,28]. The reduction conversions of $(Mn_{0.95}Si_{0.05})_2O_3$ are 71.03 % and 63.46 % after 200 and 300 cycles, respectively. Although there is still an unavoidable property degradation of the Mn-Si oxides, the evolution of the reoxidation kinetics is still faster than that of the undoped samples. In general, the cycling stability improves significantly with the introduction of Si, and the sample powder remains loose throughout the cycle without caking, while pure Mn_2O_3 powder undergoes significant shrinkage after 40 cycles, as described in the work of Bielsa et al. [25].

3.4. Surface analysis

X-ray photoelectron spectra (XPS) measurements reveal the surface composition and elemental state of samples at different reaction stages. The 5 % Si-doped sample was further studied by XPS, and full spectrum was shown in Fig. S6a, which was only composed of Mn, O, Si and C. As presented in Fig. 6a, Mn2p spectra include two peaks associated with the core $Mn2p_{3/2}$ and $Mn2p_{1/2}$ levels. Both the energy position and profile of the $Mn2p_{3/2}$ peak depend on the ionic state of Mn. Thus $Mn2p_{3/2}$ peak positions of the pure Mn_2O_3 and $(Mn_{0.95}Si_{0.05})_2O_3$ at various stages are 641.38, 641.42, 640.97, and 641.45 eV (as shown in Fig. 6a). $Mn2p_{3/2}$ peak of $(Mn_{0.95}Si_{0.05})_2O_3$ after reduction at 640.97 eV corresponds to Mn^{2+}, while the peak near 641.5 eV corresponds to Mn^{3+} [52]. Since the characteristic satellite feature of the reduced sample at 647 eV cannot be observed in Mn2p spectra, Mn3s spectra were also analyzed to aid in determining the valence of Mn ions (Shown in Fig. 6b), and the magnitude of multiplet split components of fresh and reduction samples are 5.56 and 5.98 eV, illustrating the Mn^{3+} and Mn^{2+}, respectively [53]. The corresponding O1s spectra of pure Mn_2O_3 and $(Mn_{0.95}Si_{0.05})_2O_3$ at different stages are demonstrated in Figs. S6b–c and 6c, respectively. O1s spectra possess three peaks, including lattice oxygen at ~530 eV, surface oxygen at ~531 eV assigned to defect oxide or the surface oxygen ions, and the adsorbed oxygen species at ~533 eV [54]. Table 4 shows the atom ratio of three different oxygen, the lattice oxygen content of Mn_2O_3 is 57.57 %, while those of $(Mn_{0.95}Si_{0.05})_2O_3$ at fresh, reduction, and re-oxidation stages increased to 67.78 %, 67.14 %, and 70.23 %, respectively. It is proved that the introduction of Si remarkably improved the content of lattice oxygen and made part of adsorbed oxygen transform into the lattice oxygen on the surface, which is a rate-determining step in the redox reaction [55]. In addition, adsorbed oxygen on the surface of $(Mn_{0.95}Si_{0.05})_2O_3$ also increased after the redox reaction, which may be due to the gas phase O_2 adsorb onto the surface O-vacancy to supplement the active oxygen, caused by continuous consumption of defect oxygen and lattice oxygen species during re-oxidation process [56].

TEM micrographs and SAED patterns of $(Mn_{0.95}Si_{0.05})_2O_3$ after different processes are presented in Fig. 7, while those of different stages of Mn_2O_3 are demonstrated in Fig. S8. It can be seen from Fig. 7a–c that the grains at different stages show typical coral-like morphology and are approximately 200 nm in size, which confirms the grain size of the sample calculated by XRD analysis using Scherrer's formula. Moreover, the grain boundaries are clean and clear, and amorphous or secondary phases cannot be seen. By comparing Fig. 7a and c, it was spotted that densification or coarsening did not occur after one cycle. Additionally, no evident grain size growth was found. This phenomenon may be attributed to the addition of Si elements which inhibits the sintering between grains, thus allowing the re-oxidation reaction to occur [25]. In order to prove that Si element is uniformly doped, EDS mapping was further carried out. Fig. S7 provides TEM images and corresponding EDS mapping of $(Mn_{0.95}Si_{0.05})_2O_3$ at different stages. EDS mapping graphs present homogeneous distribution of Mn and Si, indicating the synthesis of homogeneous solid solution. In addition, in the whole process of redox reaction, Si element always exists in Mn_2O_3, without local element aggregation or forming SiO_2, which further confirms Eq. (1). SAED patterns for fresh, reduction, and oxidation stages are shown in Fig. 7d–f, respectively. The diffraction patterns show the great crystalline characteristic of $(Mn_{0.95}Si_{0.05})_2O_3$, and it can be determined that the synthesized sample is monocrystal. By measuring the vector length of the projected spot to each diffraction spot and calculating the crystal plane spacing corresponding to each diffraction spot using Bragg's formula, the possible crystal plane index can be determined, and measure

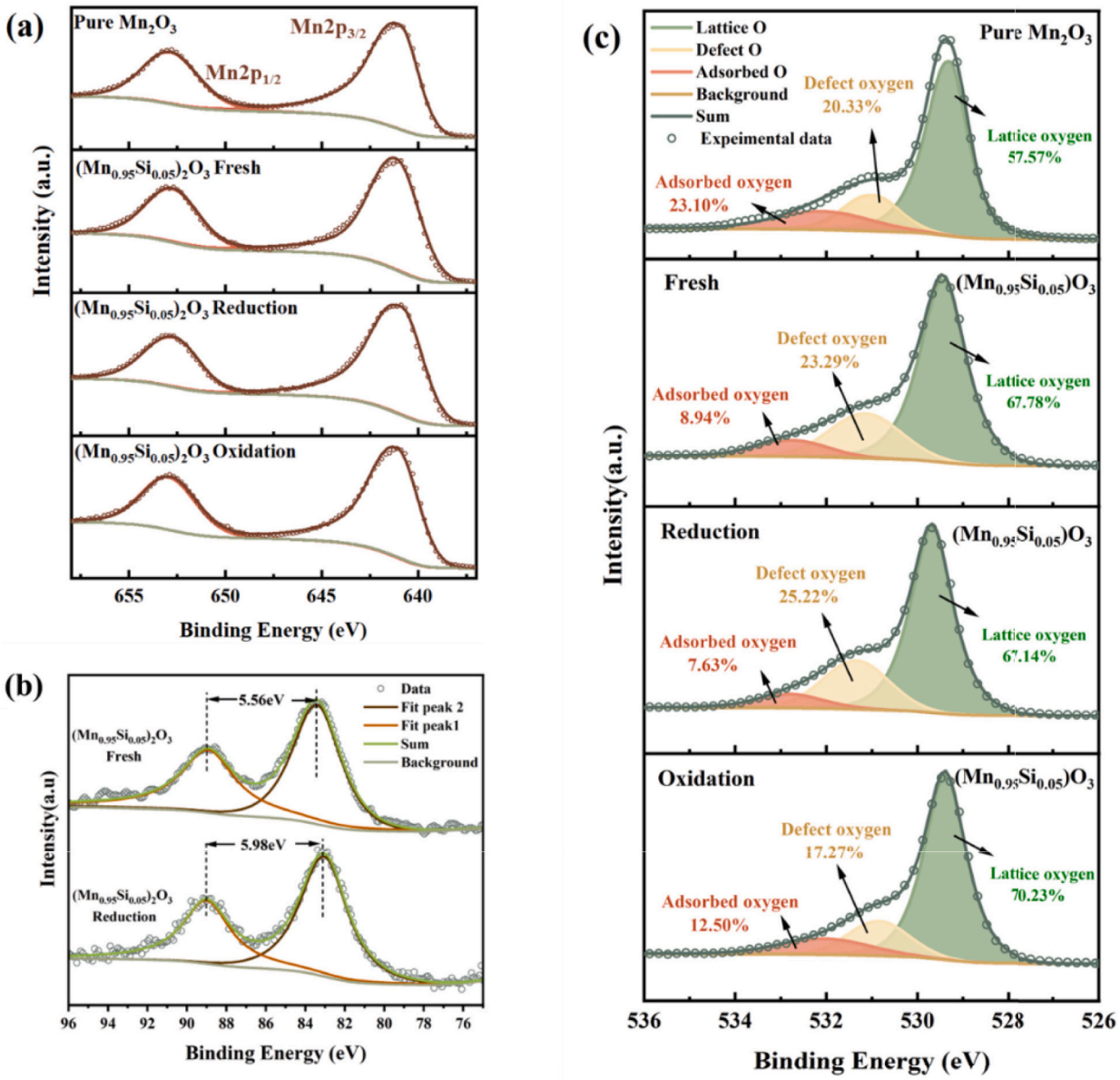

Fig. 6. XPS spectra of Mn 2p (a), Mn 3s (b) and O 1s (c).

Table 4
Oxygen species and surface molar ratio based on XPS spectra of pure Mn_2O_3 and $(Mn_{0.95}Si_{0.05})_2O_3$ at different stages.

Sample	Peak position (eV)			Surface molar ratio (%)		
	Lattice O	Defect O	Adsorbed O	Lattice O	Defect O	Adsorbed O
Mn_2O_3 fresh	529.33	531.03	532.13	57.57	20.33	23.10
Mn_2O_3 after reduction	529.58	531.03	532.09	59.37	18.70	21.93
$(Mn_{0.95}Si_{0.05})_2O_3$ fresh	529.48	531.18	532.78	67.78	23.29	8.94
$(Mn_{0.95}Si_{0.05})_2O_3$ after reduction	529.68	531.40	532.79	67.14	25.22	7.63
$(Mn_{0.95}Si_{0.05})_2O_3$ after oxidation	529.41	530.91	532.02	70.23	17.27	12.50

the vector angle between diffraction spots to determine the crystal plane (as marked in Fig. 7d–f). Corresponding crystal planes in the diffractogram are in accord with XRD patterns (As shown in Fig. 1), confirming the bixbyite as well as hausmannite of $(Mn_{0.95}Si_{0.05})_2O_3$ at different stages and their phase purity.

3.5. Si-doping modification mechanism

In this part, DFT calculations are adopted to gain a deeper insight into the manganese oxide modification mechanism by doping Si. Based on the study mentioned above of different samples, modeling and calculations are carried out here with $(Mn_{0.95}Si_{0.05})_2O_3$ as a representative to elucidate the mechanism of its improvement on the re-oxidation reaction. In the process of lattice parameters calculation, we could obtain Mn-Si composite metal oxide models with different doping ratios by replacing corresponding numbers of Mn atoms in the Mn_2O_3 (IA-3 space group) bulk model with Si atoms and the most stable site is shown in Table S1. The lattice parameters optimized by DFT are in good

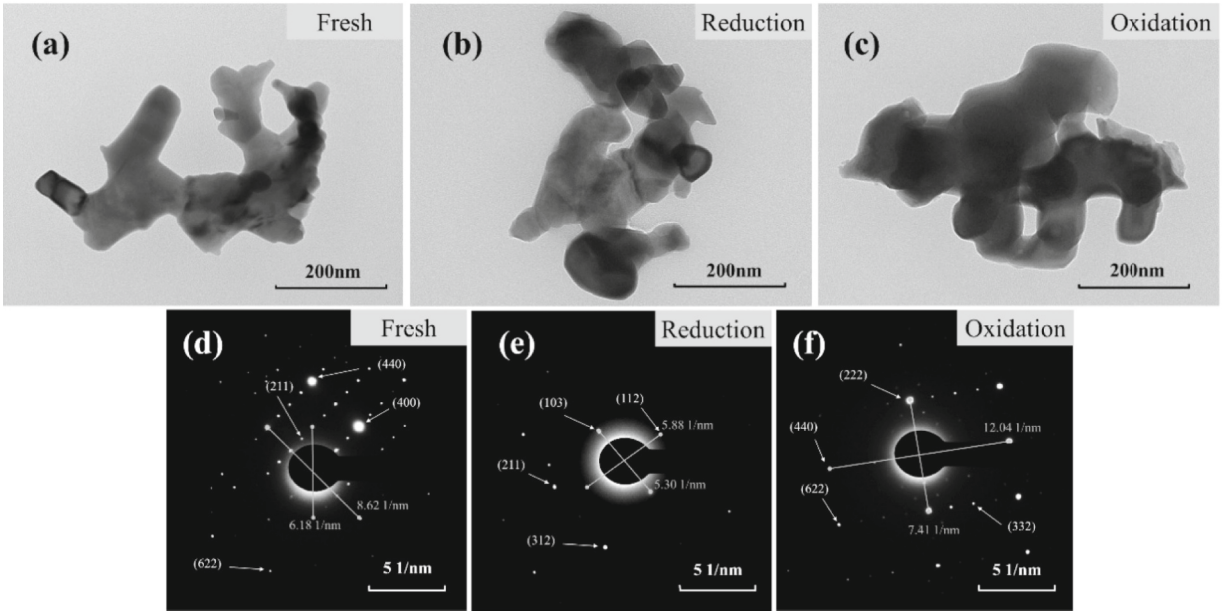

Fig. 7. TEM images and corresponding SAED images of $(Mn_{0.95}Si_{0.05})_2O_3$. (a) (d) Fresh sample, (b) (e) after reduction, (c) (f) after 1st redox cycle.

agreement with the experimental data with small deviations, as shown in Table S2.

As shown in Fig. 8a, we report the results for calculations of oxygen interactions on the reduced $(Mn_{0.95}Si_{0.05})_3O_4$ (100) slab. We studied the configurations resulting from the O_2 molecule interaction above different sites on both $(Mn_{0.95}Si_{0.05})_3O_4$ (100) and Mn_3O_4 (100) surfaces, and the most stable adsorption sites of both models were found to be located at the bridge position, as shown in Fig. 8a–b. By calculating the energy involved in O_2 adsorption ($\Delta E_{O2-Ads.}$) processes on the reduced $(Mn_{0.95}Si_{0.05})_3O_4$ (100) and Mn_3O_4 (100) surfaces, as [57]:

$$\Delta E_{O2-Ads.} = E(O_2/slab) - E(O_2) - E(slab) \quad (2)$$

In this formula, $E(O_2/slab)$ is the calculated energy for O_2/$(Mn_{0.95}Si_{0.05})_3O_4$ (100) or O_2/Mn_3O_4 (100); E(slab) is that for clean $(Mn_{0.95}Si_{0.05})_3O_4$ (100) slab or Mn_3O_4 (100) one; finally, $E(O_2)$ is the corresponding total energy for an O_2 molecule in vacuum [57]. In this way, we calculated an adsorption energy value of −2.88 eV and O—O distance of 1.41 Å, while those of Mn_3O_4 (100) were at a relatively high value of −1.13 eV and 1.43 Å, respectively. As shown in Fig. 8c, the Mn_3O_4 has a very large O_2 dissociation energy barrier (ΔE = 1.59 eV), and its final state energy is −2.88 eV, indicating an extremely sluggish oxidation step, which also explains the fact that re-oxidation processes can hardly occur. In contrast, the energy barrier ΔE of $(Mn_{0.95}Si_{0.05})_3O_4$ falls to only 0.33 eV, and the energy (−3.94 eV) is at a much lower level after oxygen dissociation, suggesting that the dissociation process has been greatly accelerated after the introduction of Si dopants. Compared with Mn_3O_4 (100) slab, our calculations indicate that M-O (M = Si or Mn) bond length in $(Mn_{0.95}Si_{0.05})_3O_4$ (100) slab shrank from 1.98 Å (for Mn-O) to 1.62 Å (for Si-O), The doping of Si changes the charge balance at the defect site, which results in the relaxation of oxygen, giving rise to changes in the lattice constant as well as lattice strain.

As shown in Fig. 9b, the oxygen vacancy formation $E(V_O)$ and the migration energy barriers of $(Mn_{0.95}Si_{0.05})_3O_4$ (100) plates in the first and second atomic layers were calculated in order to further investigate the diffusion of oxygen ions within the lattice, using Mn_3O_4 (100) as a reference. The oxygen vacancy formation energy $E(V_O)$ is calculated as follows:

$$E(V_O) = E(slab/V_O) + 1/2E(O_2) - E(slab) \quad (3)$$

where: $E(slab/V_O)$ and E(slab) are the energies of the relaxed surfaces slabs with and without oxygen vacancy, respectively, and $E(O_2)$ is the energy of the oxygen molecule in vacuum. With this, the calculation values of the V_O at the first layer and the second layer of $(Mn_{0.95}Si_{0.05})_3O_4$ (100) are about 1.24 eV and 1.36 eV, respectively, and this value is lower than that of 2.03 eV and 2.75 eV for Mn_3O_4 (100). The calculated Mn—O bond length near Si in the lattice of $(Mn_{0.95}Si_{0.05})_3O_4$ (100) increases to 2.29 Å, while the Mn—O bond length in undoped Mn_2O_3 is 1.98 Å. The Mn—O bond breaks more easily and the oxygen vacancy formation energy is reduced, and the hypothesis is based on the fact that longer Mn—O bonds will be easier to break and rearrange than shorter bonds [50] , indicating that the Mn—O bond is weakened by the Si cation. The oxygen ion migration process of $(Mn_{0.95}Si_{0.05})_3O_4$ (100) slab is shown in Fig. 9a, while that of Mn_3O_4 (100) is presented in Fig. S9. Especially, as shown in Fig. 9b, the energy barrier reduces from 2.90 eV for Mn_3O_4 (100) to 0.22 eV for $(Mn_{0.95}Si_{0.05})_3O_4$ (100), indicating the higher activity for oxygen ion migration in $(Mn_{0.95}Si_{0.05})_3O_4$. After the oxidation reaction continues for some time when the surface is completely covered with oxidation products, oxygen must diffuse within the lattice of the oxidation product layers. Therefore, the oxygen vacancy formation energy and migration energy barriers of Mn_2O_3 and $(Mn_{0.95}O_{0.05})_2O_3$ were calculated. As shown in Fig. S10, the oxygen vacancy formation energy of both the first and second layers of Mn_2O_3 is higher than that of $(Mn_{0.95}O_{0.05})_2O_3$, indicating that it is theoretically easier to form oxygen vacancy defects in $(Mn_{0.95}O_{0.05})_2O_3$. Calculations show that the energy barriers for oxygen vacancy migration in Mn_2O_3 and $(Mn_{0.95}O_{0.05})_2O_3$ are 1.79 eV and 0.56 eV, respectively, which indicates that that the lattice diffusion of O^{2-} in Mn-Si oxides is also more likely to occur during the product layer diffusion phase than before doping.

Thus, the defects resulting from Si-doped reduce the diffusion barrier of ions in the crystal, which increases the diffusion rate of ions, conducive to the occurrence of gas-solid reaction in the re-oxidation process. All these calculations theoretically elucidate that introducing the Si dopant can effectively ameliorate the poor reaction kinetics of re-oxidation caused by obstructed oxygen diffusion and significantly improve the heat and mass transfer properties of heat storage materials.

Based on the experimental analyses and DFT calculations presented above, a possible modification mechanism by doping Si element in Mn_2O_3/Mn_3O_4 couple was proposed and is shown in Fig. 10. In the reduction process, when the Mn-based composite metal oxide thermal storage material $(Mn_{1-x}Si_x)_2O_3$ is excited by sunlight or external energy,

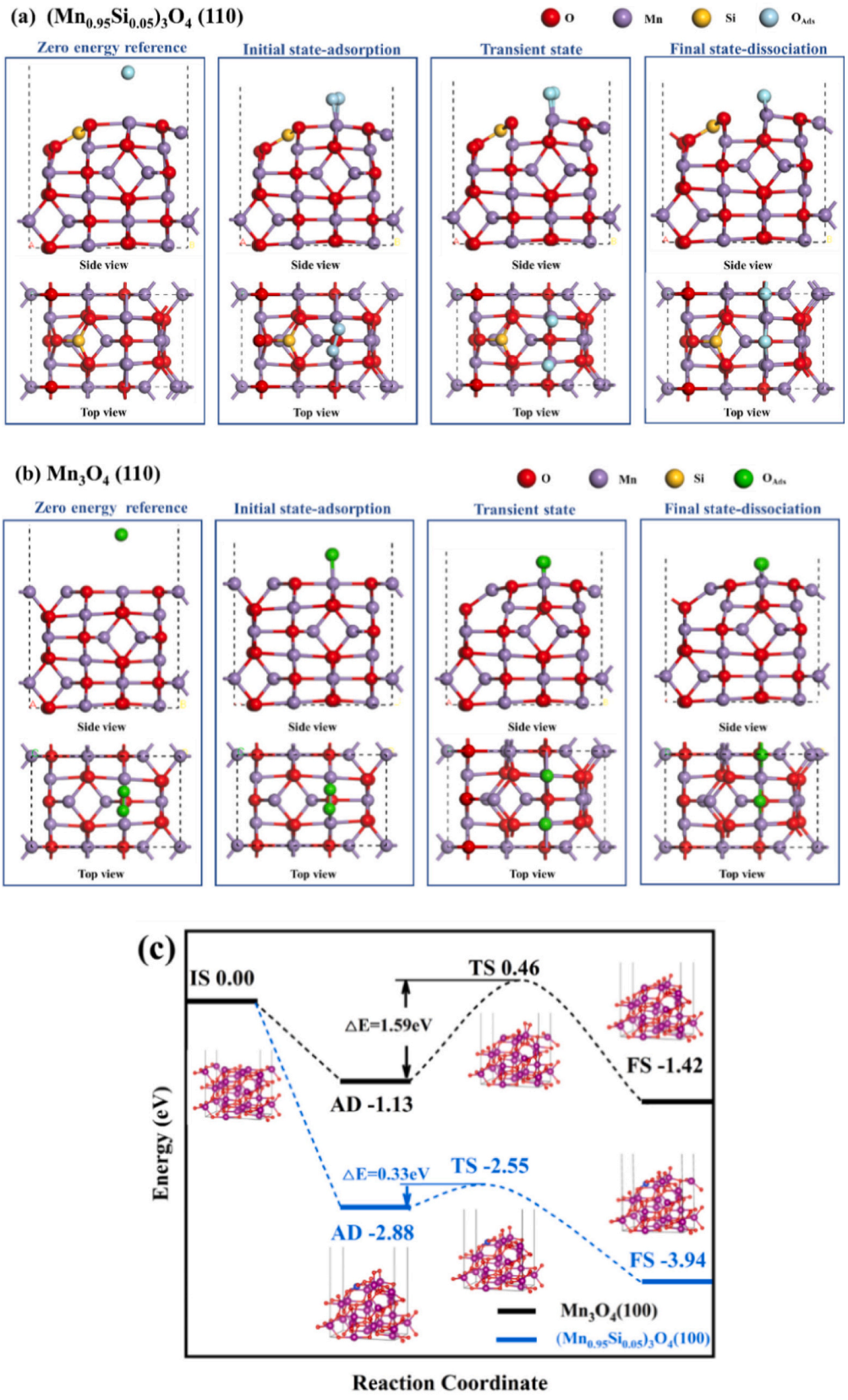

Fig. 8. Oxygen adsorption and dissociation process. (a) The O_2/$(Mn_{0.95}Si_{0.05})_3O_4$ (100) system with a dioxygen species adsorbed on hollow site and dissociation process. (b) The O_2/Mn_3O_4 (100) system with a dioxygen species adsorbed on hollow site and dissociation process. (c) Oxygen adsorption/dissociation potential energy diagram.

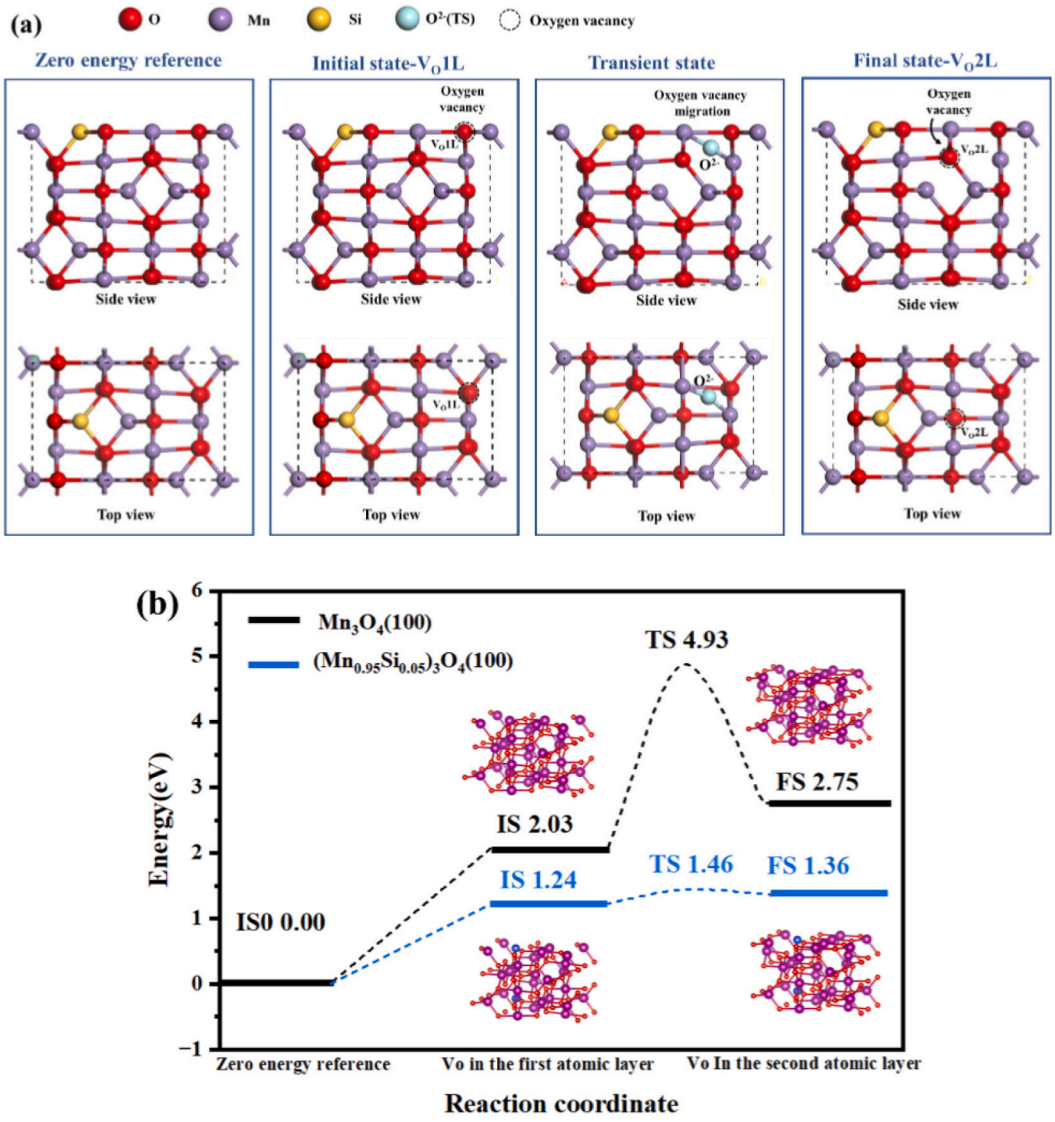

Fig. 9. (a) Top and side view of $(Mn_{0.95}Si_{0.05})_3O_4$ geometric structures at different state during oxygen ions migration. (b) The formation energies of oxygen vacancies E(V_O) at different sites of $(Mn_{0.95}Si_{0.05})_3O_4$ (100) slab and Mn_3O_4 (100) and energy barriers of migration.

surface lattice oxygen ions desorb and diffuse outward to form oxygen molecules. To maintain charge balance, more inner Mn—O bonds are broken by free electrons and more oxygen ions are driven to migrate outward [20]. At this point, the Mn^{3+} ions transform into Mn^{2+} and regenerate into $(Mn_{1-x}Si_x)_3O_{4-\delta}$. In re-oxidation, the oxygen molecules are adsorbed and dissociated into O ions, which migrate to the surface oxygen vacancies and disrupt the local charge balance. The introduction of Si reduces the adsorption/dissociation energy of oxygen molecules and the migration energy barrier of oxygen vacancies in the reduced and re-oxidized products, increasing the migration rate of oxygen ions within the lattice. In this way, the emergence-annihilation of oxygen vacancy defects during the oxidation process can be easily achieved [58], thus enhancing the oxidation reaction activity.

4. Conclusions

The purpose of the current work is to propose a cheap and environmentally friendly modified Mn-Si composite metal oxide $(Mn_{1-x}Si_x)_2O_3$ and investigate its performance enhancement mechanism. Mn_2O_3/Mn_3O_4 redox pair was highly researched as a thermochemical thermal storage material because of its cheap and non-toxic character, but the poor reaction kinetics triggered by sintering limited its practical application and development. In this study, the homogeneous solid solution was obtained by substituting Si into the lattice of Mn_2O_3, which exhibited excellent reversibility and cyclic stability. Samples with different Si ratios from 1 to 15 % were synthesized by sol-gel method for comparison, and it was found that $(Mn_{0.97}Si_{0.03})_2O_3$ and $(Mn_{0.95}Si_{0.05})_2O_3$ exhibited the best performances, showing re-oxidation conversion rate of 90.29 % and 86.18 %, respectively, in the first cycle. The measured thermal storage density of $(Mn_{0.97}Si_{0.03})_2O_3$ is 189.8 kJ/kg, close to the theoretical value of 202 kJ/kg for Mn_2O_3. Cycling tests were performed to evaluate the cycling stability of $(Mn_{0.95}Si_{0.05})_2O_3$, and the reduction conversion remained above 90 % after 50 cycles and was 63.64 % after 300 cycles. A small amount of doping (<5 mol%) does not seriously affect the microstructure, including grain size and specific surface area. However, Si^{4+} doping at the atomic scale causes lattice distortion, which triggers defects and elevates the ratio of lattice oxygen and defects oxygen. Based on density functional theory, it is found that the reaction barrier of surface oxygen adsorption and oxygen dissociation decreases obviously after doping. Moreover, the oxygen vacancy formation energy is reduced, and the oxygen migration energy barrier inside the crystal is also substantially lower than that of pure Mn_2O_3,

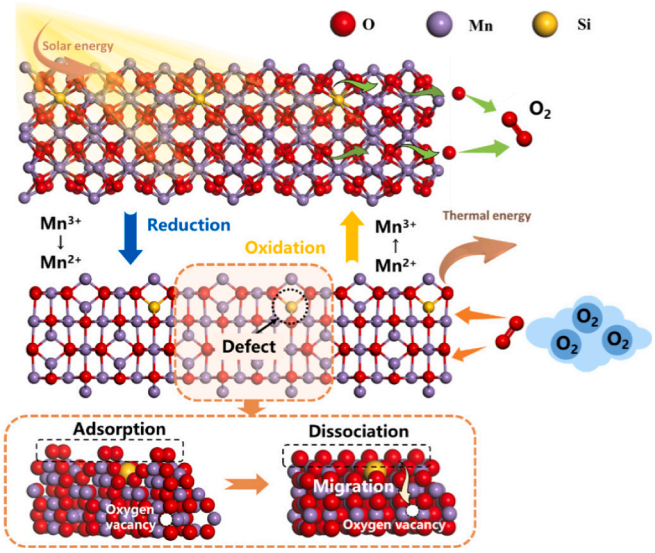

Fig. 10. Schematic of the modification mechanism by displacement doping Si.

which explains the re-oxidation reaction that occurs more easily in $(Mn_{1-x}Si_x)_3O_4$ under the same conditions. The introduction of Si enables the Mn_2O_3/Mn_3O_4 pair to react efficiently and reversibly, providing an economical option for future thermochemical energy storage materials for the next generation of concentrated solar power plants.

CRediT authorship contribution statement

Y.H. was responsible for conceptualization, methodology, software, investigation, and writing the original draft. P.Z. reviewed and edit the manuscript. C.G. validated the study and wrote, reviewed, and edited the manuscript. H.X. visualized the experiment and wrote, reviewed, and edited the manuscript. J.Z. was responsible for the resources, project administration, and funding acquisition. G.X. was responsible for the resources, supervision, project administration, and funding acquisition.

Declaration of competing interest

The authors declare that they have no known competing financial interests or personal relationships that could have appeared to influence the work reported in this paper.

Data availability

Data will be made available on request.

Acknowledgment

This work was supported by the National Natural Science Foundation of China (52176207), the Zhejiang Provincial Natural Science Foundation (LR20E060001), and the Fundamental Research Funds for the Central Universities (2022ZFJH04).

Appendix A. Supplementary data

Details of TGA-DSC measurements, phase diagram, FTIR spectra, XPS spectra, SEM-EDS mapping, statistics of particle size distribution, and DFT calculations. Supplementary data to this article can be found online at https://doi.org/10.1016/j.est.2023.108804.

References

[1] A.J. Carrillo, J. González-Aguilar, M. Romero, J.M. Coronado, Solar energy on demand: a review on high temperature thermochemical heat storage systems and materials, Chem. Rev. 119 (7) (2019) 4777.
[2] L.A. Weinstein, J. Loomis, B. Bhatia, D.M. Bierman, E.N. Wang, G. Chen, Concentrating solar power, Chem. Rev. 115 (23) (2015) 12797.
[3] H. Zhang, J. Baeyens, G. Cáceres, J. Degrève, Y. Lv, Thermal energy storage: recent developments and practical aspects, Prog. Energy Combust. Sci. 53 (2016) 1.
[4] S. Wu, C. Zhou, E. Doroodchi, R. Nellore, B. Moghtaderi, A review on high-temperature thermochemical energy storage based on metal oxides redox cycle, Energy Convers. Manag. 168 (2018) 421.
[5] C. Agrafiotis, M. Roeb, C. Sattler, Exploitation of thermochemical cycles based on solid oxide redox systems for thermochemical storage of solar heat. Part 4: screening of oxides for use in cascaded thermochemical storage concepts, Sol. Energy 139 (2016) 695.
[6] A.J. Schrader, A.P. Muroyama, P.G. Loutzenhiser, Solar electricity via an Air Brayton cycle with an integrated two-step thermochemical cycle for heat storage based on Co3O4/CoO redox reactions: thermodynamic analysis, Sol. Energy 118 (2015) 485.
[7] S. Tescari, A. Singh, C. Agrafiotis, L. de Oliveira, S. Breuer, B. Schlögl-Knothe, M. Roeb, C. Sattler, Experimental evaluation of a pilot-scale thermochemical storage system for a concentrated solar power plant, Appl. Energy 189 (2017) 66.
[8] M. Deutsch, F. Horvath, C. Knoll, D. Lager, C. Gierl-Mayer, P. Weinberger, F. Winter, High-temperature energy storage: kinetic investigations of the CuO/Cu2O reaction cycle, Energy Fuel 31 (3) (2017) 2324.
[9] M. Gigantino, S. Sas Brunser, A. Steinfeld, High-temperature thermochemical heat storage via the CuO/Cu2O redox cycle: from material synthesis to packed-bed reactor engineering and cyclic operation, Energy Fuel 34 (12) (2020) 16772.
[10] S. Setoodeh Jahromy, F. Birkelbach, C. Jordan, C. Huber, M. Harasek, A. Werner, F. Winter, Impact of partial pressure, conversion, and temperature on the oxidation reaction kinetics of Cu2O to CuO in thermochemical energy storage, Energies 12 (3) (2019).
[11] A.J. Carrillo, D.P. Serrano, P. Pizarro, J.M. Coronado, Thermochemical heat storage based on the Mn2O3/Mn3O4redox couple: influence of the initial particle size on the morphological evolution and cyclability, J. Mater. Chem. A 2 (45) (2014) 19435.
[12] Alonso, E.; Gallo, A.; Pérez-Rábago, C.; Fuentealba, E., 2016, DOI:https://doi.org/10.1063/1.4949102.
[13] D. Xiang, C. Gu, H. Xu, J. Deng, P. Zhu, G. Xiao, Al-modified CuO/Cu2O for high-temperature thermochemical energy storage: from reaction performance to modification mechanism, ACS Appl. Mater. Interfaces 13 (48) (2021) 57274.
[14] C. Agrafiotis, S. Tescari, M. Roeb, M. Schmücker, C. Sattler, Exploitation of thermochemical cycles based on solid oxide redox systems for thermochemical storage of solar heat. Part 3: cobalt oxide monolithic porous structures as integrated thermochemical reactors/heat exchangers, Sol. Energy 114 (2015) 459.
[15] B. Wong, Thermochemical Heat Storage for Concentrated Solar Power, 2011.
[16] A.J. Carrillo, D.P. Serrano, P. Pizarro, J.M. Coronado, Improving the thermochemical energy storage performance of the Mn2O3/Mn3O4 redox couple by the incorporation of iron, ChemSusChem 2015 (1947) 8.
[17] S. Project, Thermochemical Heat Storage for Concentrated Solar Power, 2011.
[18] W. Huang, D. Korba, K. Randhir, J. Petrasch, J. Klausner, N. AuYeung, L. Li, Thermochemical reduction modeling in a high-temperature moving-bed reactor for energy storage: 1D model, Appl. Energy 306 (2022).
[19] J. Fan, Y. Zhang, Y. Yang, J. Hao, Y. Wang, A. Qian, Performance of thermochemical energy storage for spinel CuMn2O4 material, J. Energy Storage (2021) 41.
[20] D. Xiang, C. Gu, H. Xu, G. Xiao, Self-assembled structure evolution of MnFe oxides for high temperature thermochemical energy storage, Small 17 (29) (2021), e2101524.
[21] K. Randhir, K. King, N. Rhodes, L. Li, D. Hahn, R. Mei, N. Auyeung, J. Klausner, Magnesium-manganese oxides for high temperature thermochemical energy storage, J. Energy Storage 21 (2019) 599.
[22] K. King, K. Randhir, J. Klausner, Calorimetric method for determining the thermochemical energy storage capacities of redox metal oxides, Thermochim. Acta 673 (2019) 105.
[23] K. Randhir, M. Hayes, P. Schimmels, J. Petrasch, J. Klausner, Zero carbon solid-state rechargeable redox fuel for long duration and seasonal storage, Joule 6 (11) (2022) 2513.
[24] N.W. Hlongwa, D. Sastre, E. Iwuoha, A.J. Carrillo, C. Ikpo, D.P. Serrano, P. Pizarro, J.M. Coronado, Exploring the thermochemical heat storage capacity of AMn2O4 (A = Li or Cu) spinels, Solid State Ionics 320 (2018) 316.
[25] D. Bielsa, A. Zaki, P.L. Arias, A. Faik, Improving the redox performance of Mn2O3/Mn3O4 pair by Si doping to be used as thermochemical energy storage for concentrated solar power plants, Sol. Energy 204 (2020) 144.
[26] A. Shulman, E. Cleverstam, T. Mattisson, A. Lyngfelt, Manganese/iron, manganese/nickel, and manganese/silicon oxides used in chemical-looping with oxygen uncoupling (CLOU) for combustion of methane, Energy Fuel 23 (10) (2009) 5269.
[27] D. Yilmaz, E. Darwish, H. Leion, Investigation of the combined Mn-Si oxide system for thermochemical energy storage applications, J. Energy Storage (2020) 28.
[28] D. Bielsa, A. Zaki, P.L. Arias, A. Faik, Development of a kinetic reaction model for reduction and oxidation of Si doped Mn2O3 for thermochemical energy storage in concentrated solar power plants, J. Energy Storage (2021) 43.
[29] G. Kresse, J. Furthmüller, Efficiency of ab-initio total energy calculations for metals and semiconductors using a plane-wave basis set, Comput. Mater. Sci. 6 (1) (1996) 15.

[30] G. Kresse, J. Hafner, Abinitio molecular-dynamics for liquid-metals, Phys. Rev. B Condens. Matter 47 (1) (1993) 558.
[31] G. Kresse, D. Joubert, From ultrasoft pseudopotentials to the projector augmented-wave method, Phys. Rev. B Condens. Matter 59 (3) (1999) 1758.
[32] J.P. Perdew, K. Burke, M. Ernzerhof, Generalized gradient approximation made simple, Phys. Rev. Lett. 77 (18) (1996) 3865.
[33] H.J. Monkhorst, J.D. Pack, Special points for Brillouin-zone integrations, Phys. Rev. B Condens. Matter 13 (12) (1976) 5188.
[34] V.I. Anisimov, J. Zaanen, O.K. Andersen, Band theory and Mott insulators: Hubbard U instead of Stoner I, Phys. Rev. B Condens. Matter 44 (3) (1991) 943.
[35] S.L. Dudarev, G. Botton, S.Y. Savrasov, C.J. Humphreys, A.P. Sutton, Electron-energy-loss spectra and the structural stability of nickel oxide: an LSDA+U study, Phys. Rev. B Condens. Matter 57 (3) (1998) 1505.
[36] A. Zaki, J. Carrasco, D. Bielsa, A. Faik, Tunable redox temperature of a Co3-xMnxO4 (0 </= x </= 3) continuous solid solution for thermochemical energy storage, ACS Appl. Mater. Interfaces 12 (6) (2020) 7010.
[37] B.M. Reddy, G. Thrimurthulu, L. Katta, Y. Yamada, S.-E. Park, Structural characteristics and catalytic activity of nanocrystalline ceria-praseodymia solid solutions, J. Phys. Chem. C 113 (2009) 15882–15890.
[38] F. Gong, S. Lu, L. Peng, J. Zhou, J. Kong, D. Jia, F. Li, Hierarchical Mn(2)O(3) microspheres in-situ coated with carbon for supercapacitors with highly enhanced performances, Nanomaterials (Basel) 7 (12) (2017).
[39] A. Aridi, R. Awad, A. Khalaf, Synthesis and characterization of ZnFe2O4/ Mn2O3 nanocomposites, Appl. Phys. A 127 (3) (2021).
[40] M.T. Kim, Deposition behavior of hexamethyldisiloxane films based on the FTIR analysis of Si-O-Si and Si-CH3 bonds, Thin Solid Films 311 (1–2) (1997) 157.
[41] M.D. Alba, Z. Luan, J. Klinowski, Titanosilicate mesoporous molecular sieve MCM-41: synthesis and characterization, J. Phys. Chem. (1952) 100 (6) (1996) 2178.
[42] S. Schwarz, D.R. Corbin, A.J. Vega, The band at “960”, Microporous Macroporous Mater. 431 (1996) 137.
[43] Z.Y. Yuan, S.Q. Liu, T.H. Chen, J.Z. Wang, H.X. Li, Synthesis of iron-containing MCM-41, J. Chem. Soc. Chem. Commun. 10.1039/C39950000973(9) (1995) 973, https://doi.org/10.1039/C39950000973.
[44] L.-z. Wang, J.-l. Shi, J. Yu, D.-s. Yan, Synthesis of nanostructured mesoporous silica materials containing manganese, Nanostruct. Mater. 10 (8) (1998) 1289.
[45] M. Ishii, M. Nakahira, T. Yamanaka, Infrared absorption spectra and cation distributions in (Mn, Fe)3O4, Solid State Commun. 11 (1) (1972) 209.
[46] S. Ashoka, G. Nagaraju, G.T. Chandrappa, Reduction of KMnO4 to Mn3O4 via hydrothermal process, Mater. Lett. 64 (22) (2010) 2538.
[47] A. Askarinejad, A. Morsali, Direct ultrasonic-assisted synthesis of sphere-like nanocrystals of spinel Co3O4 and Mn3O4, Ultrason. Sonochem. 16 (1) (2009) 124.
[48] L. André, S. Abanades, L. Cassayre, High-temperature thermochemical energy storage based on redox reactions using Co-Fe and Mn-Fe mixed metal oxides, J. Solid State Chem. 253 (2017) 6.
[49] M. Rydén, H. Leion, T. Mattisson, A. Lyngfelt, Combined oxides as oxygen-carrier material for chemical-looping with oxygen uncoupling, Appl. Energy 2014 (1924) 113.
[50] A.J. Carrillo, D.P. Serrano, P. Pizarro, J.M. Coronado, Understanding redox kinetics of iron-doped manganese oxides for high temperature thermochemical energy storage, J. Phys. Chem. C 120 (49) (2016) 27800.
[51] F. García-Labiano, L.F. de Diego, J. Adánez, A. Abad, P. Gayán, Reduction and oxidation kinetics of a copper-based oxygen carrier prepared by impregnation for chemical-looping combustion, Ind. Eng. Chem. Res. 43 (26) (2004) 8168.
[52] Y. Fang, Y. Wang, F. Wang, J. Zhu, 3D structured Mn2O3 synthesized using tween surfactant: influence on the morphology and oxygen reduction catalytic performance, CrystEngComm 21 (3) (2019) 420.
[53] M. Fujiwara, T. Matsushita, S. Ikeda, Evaluation of Mn3s X-ray photoelectron spectroscopy for characterization of manganese complexes, J. Electron Spectrosc. Relat. Phenom. 74 (3) (1995) 201.
[54] X. Lin, S. Li, H. He, Z. Wu, J. Wu, L. Chen, D. Ye, M. Fu, Evolution of oxygen vacancies in MnOx-CeO2 mixed oxides for soot oxidation, Appl. Catal. B Environ. 223 (2018) 91.
[55] Z. Zhang, J. Yu, J. Zhang, Q. Ge, H. Xu, F. Dallmann, R. Dittmeyer, J. Sun, Tailored metastable Ce-Zr oxides with highly distorted lattice oxygen for accelerating redox cycles, Chem. Sci. 9 (13) (2018) 3386.
[56] V. Rico-Pérez, E. Aneggi, A. Bueno-López, A. Trovarelli, Synergic effect of Cu/Ce0.5Pr0.5O2-δ and Ce0.5Pr0.5O2-δ in soot combustion, Appl. Catal. B Environ. 197 (2016) 95.
[57] B. Milberg, A. Juan, B. Irigoyen, Redox behavior of a low-doped Pr-CeO2(111) surface. A DFT+U study, Appl. Surf. Sci. 401 (2017) 206.
[58] P. Wang, J. Wang, X. An, J. Shi, W. Shangguan, X. Hao, G. Xu, B. Tang, A. Abudula, G. Guan, Generation of abundant defects in Mn-Co mixed oxides by a facile agar-gel method for highly efficient catalysis of total toluene oxidation, Appl. Catal. B Environ. 282 (2021).